Hot corrosion behavior of additively manufactured stainless steel 316L and Inconel 718 in MgCl$_2$/KCl/NaCl chloride salts at 700 °C

Hao Shi[a, b, *], Tao Wu[c, *], Qing Gong[d], Wenjin Ding[d, *], Yan Chai[d], Alfons Weisenburger[a], Litao Chang[e], Zhao Zhang[f], Kangli Wang[b], Julia Richter[c], Thomas Niendorf[c], Georg Müller[a]

[a]*Institute for Pulsed Power and Microwave Technology (IHM), Karlsruhe Institute of Technology (KIT), Hermann-von-Helmholtz-Platz 1, 76344 Eggenstein-Leopoldshafen, Germany*

[b]*State Key Laboratory of Advanced Electromagnetic Engineering and Technology, School of Electrical and Electronic Engineering, Huazhong University of Science and Technology, Wuhan 430074, PR China*

[c] *Institute of Materials Engineering, University of Kassel, Möchebergstr. 3, 34125 Kassel, Germany*

[d] *Institute of Engineering Thermodynamics, German Aerospace Center (DLR), 70569 Stuttgart, Germany*

[e] *Shanghai Institute of Applied Physics, Chinese Academy of Sciences, Shanghai, China 201800*

[f] *State Key Laboratory of Structural Analysis for Industrial Equipment, Dalian University of Technology, Dalian, China*

*Corresponding author. E-mail address: h.shi@mpie.de (H.Shi); wutao202@hotmail.com (T.Wu); wenjin.ding@dlr.de (W.J. Ding).

Abstract

Two additively manufactured (AM) materials, i.e., stainless steel 316L (SS316L) and Ni-base superalloy Inconel 718 (IN718), have been exposed to MgCl$_2$-KCl-NaCl (47.1-22.7-30.2 mol%) salts at 700 °C to investigate their corrosion behavior. Corrosion tests were conducted using SS316L processed by laser metal deposition (LMD), IN718 by laser powder bed fusion (PBF-LB) as well as conventionally processed counterparts. The obtained results reveal that LMD SS316L is characterized by inferior corrosion resistance, mainly due to the segregation of δ-ferrite at grain boundary (GB). Two different types of corrosion morphologies, uniform corrosion and GB-driven corrosion, are observed in both AM and the conventionally processed IN718 samples. The GB-driven corrosion is accelerated by the evolution of δ-phase in case of IN718.

Keywords: Additive manufacturing, 3D printing; Corrosion; Microstructure; Molten salts, austenitic stainless steel 316L, Inconel 718.

1. Introduction

Molten chloride salt, with the chemical composition (MgCl$_2$-KCl-NaCl, 47.1-22.7-30.2 mol%, eutectic), has been proposed as heat transfer/storage medium because of three main advantages, namely low price (< 0.35 $/kg), low melting point (< 400 °C), and high thermal stability (> 800 °C) [1-2]. By increasing the operating temperature of molten chlorides based thermal energy storage (TES), the energy conversion efficiency will be improved in terms of reduced Levelized Cost of Electricity (LCOE) [3]. However, molten chloride salts mixture, usually containing alkaline earth metal chloride salts (e.g. MgCl$_2$, CaCl$_2$), is strongly corrosive to Fe- or Ni- based structural steels/superalloys [2-8].

Moreover, the corrosion is further enhanced by increasing the operation temperature [9-10]. Previous studies show that the corrosion is mainly driven by impurities, like $MgOH^+$ (i.e. $MgOH^+Cl^-$), O_2, Cl_2 and HCl from the salts [4-14]. Further information on this topic can be found in a recent review paper [13]. Corrosion features like Cr depletion, corrosion pores, MgO deposition in the corroded layer, material loss, and oxide layer formation have been reported [2-11]. Generally, Ni-based superalloys are more corrosion resistant than Fe-based steels [4-7, 10, 12]. Besides, some corrosion mitigation strategies like adding pure Mg inhibitor, pre-oxidation of steels/superalloys or salts purification have been proposed and investigated [9, 11, 14-16]. However, the complex structure of some components of the system, namely pump and sealing parts, make the conventional steel production and corrosion protection become challenging in such an environment [2-3].

Additive manufacturing (AM), also referred to as 3D printing, is a novel manufacturing process. Complex parts are realised based on layer-wise joining of precursor materials, i.e., powders or wires, directly from the 3D model data [17-18]. As compared to traditional metallic material production, AM has its advantages like the direct production of parts without tooling, a high freedom of design for complex structures and an efficient use of materials [17-19]. It has been considered as a replacement of the traditional manufacturing in varies of industry fields, like aerospace, automobile industry, energy and nuclear industry [20-23]. Laser powder bed fusion (PBF-LB) also known as selective laser melting (SLM), and laser metal deposition (LMD) also termed to as direct laser deposition (DLD) or directed energy deposition (DED), are two widely used methods for AM [17-19]. Stainless steel 316L (SS316L) and Ni-base superalloy Inconel 718 (IN718) are widely studied in AM being characterised by promising corrosion and mechanical properties [17, 19, 22-26]. Compared to wrought SS316L, the microstructure of AM SS316L exhibits different characteristics regarding the texture and grain size, which are highly dependent on the manufacturing approach applied. For instance, SS316L processed by PBF-LB is fully austenitic while the LMD process promotes segregations at grain boundaries (GBs), like Cr- and Mo-enriched precipitates at sub-grain boundaries and intercellular δ-ferrite formation, respectively [20, 27, 28]. In case of IN718, the face-centred cubic (FCC) γ-matrix usually contains diverse precipitates like Laves-phase, γ'/γ''-phase and δ-phase ($NbNi_3$) [24, 25, 29]. The specific volume fractions of these precipitates are strongly affected by the process parameters in AM. Furthermore, it has been revealed that the precipitation in AM manufactured Ni-base superalloys generally proceeds faster than in conventionally processed counterparts [30]. Besides, inclusions like MnS and oxides, carbides, pores and lack of fusions are common defects of AM materials, which are known to have influence on the corrosion behavior [17, 19, 22-31].

Up to now, no literature reports the corrosion behavior of LMD SS316L and PBF-LB IN718 when exposed to molten chloride salts. Relevant corrosion tests of wrought/forged SS316L and IN718 in molten chloride salts indicate their promising corrosion performance [6, 29]. One study by Sun et al.

[6] has clarified the corrosion behavior of SS316L in NaCl-KCl-MgCl$_2$ (33–21.6–45.4 mol%) at 700 °C under N$_2$ atmosphere. A corrosion depth around 40 µm has formed after 100 h exposure time. In addition to the Cr depletion in the corroded zone, intergranular corrosion attack was observed. Zhuang et al. [32] evaluated the corrosion behavior of IN718 in eutectic mixture of NaCl-KCl-ZnCl$_2$ (8.1–31.3–60.6 wt.%) and revealed its promising corrosion resistance under such condition. Some features of exposed samples like Cr-depletion, oxides formation and mass loss have been observed. This is also reflected by exposing the IN718 to molten alkali fluoride salts [33].

Since the AM materials possess unique microstructures compared to the conventionally manufactured counterparts, it is interesting to investigate the corrosion mechanism of LMD SS316L and PBF-LB IN718 exposed to molten MgCl$_2$-KCl-NaCl (47.1-22.7-30.2 mol%). Besides, it is essential to understand the influence of second phases, precipitates and GBs on the corrosion behavior of bulk material. As a reference, two commercial/wrought SS316L and IN718 reference conditions are exposed in the same manner. The obtained results will help understand the corrosion behavior of AM materials in molten chloride salts with respect to process-inherent features like defects and unique microstructures.

2. Materials and methods

2.1 Material preparation

In the present work, two well-known types of alloys, i.e., SS316L and IN718, were selected for the corrosion exposure in molten chloride salts. They were processed by LMD and PBF-LB, respectively. The objective of choosing different alloys with different manufacturing techniques is to provide a broad understanding of the mechanisms and response of alloys suffering from corrosion environment. Table 1 displays the chemical compositions of the feedstock materials used for AM. As a reference, conventionally processed SS316L and IN718 alloys were also exposed to the same condition. The chemical compositions of the reference commercial alloys were measured by electron dispersive X-ray spectroscopy (EDS, error bar of 1 wt.%) and can be found in Table 1 as well.

The IN718 samples were manufactured using a SLM 280^{HL} system (SLM Solutions Group AG, Lübeck, Germany) equipped with two lasers with nominal powers of 400 W and 1000 W. The parameters followed standard procedures are detailed in a previous work [34]. During the build process, the whole build chamber was flooded with shielding gas (Ar, purity > 99.999 %) to establish an inert process gas atmosphere to avoid oxidation during the melting process. IN718 alloy powder with particle sizes in the range of 15-53 µm were used [34]. During the process the platform was heated to 200 °C. IN718 cuboid specimens with dimensions of 10 mm × 10 mm × 40 mm were fabricated, see Fig. 1(a), and then used for the corrosion tests (information on corrosion tests will be provided in Section 2.2). A bi-directional scanning strategy with 67° rotation for every consecutive layer was utilized.

The SS316L parts were fabricated using the LMD technology. The system consisted of a Kuka six-

axes robot (ZH 30/60III), a Laser Line diode laser generator (LMD 4000-100) with 4000 W maximum power, a Precitec laser cladding head (YC52) with four coaxial nozzles, and a Raychem metal powder feeder (RC-PGF-D). The powder of SS316L with sizes of 45-150 μm and spherical shape, produced by Höganäs, was laser deposited on a SS316L substrate with the dimensions of 130 mm × 40mm × 15 mm. Pure Ar with 99.99 % purity was used as carrier and shielding gas in all processes at flow rates of 400 L/h and 600 L/h, respectively. The process parameters adopted are given as follows: laser peak power of 1000 W, scanning speed of 6 mm/s, powder feed rate of 6 mm/s, T-pulse of 25 ms and Z-increment of 0.2 mm between two layers for all deposited parts. The dimensions of the samples were 60 mm × 10 mm × 40 mm. A bi-directional scanning strategy without rotation for every layer was used. Small samples with dimensions of 10 mm × 2 mm × 30 mm were cut from the initial LMD sample and used for corrosion testing. Further information on the dimensions of the sample and the actual scanning strategy can be found in Figure 1(b).

Table 1
Chemical compositions of AM alloy powders used in present work, commercial SS316L and IN718. All materials were characterised by EDS (wt.%) (Com SS316L: commercial SS316L; Com IN718: commercial IN718).

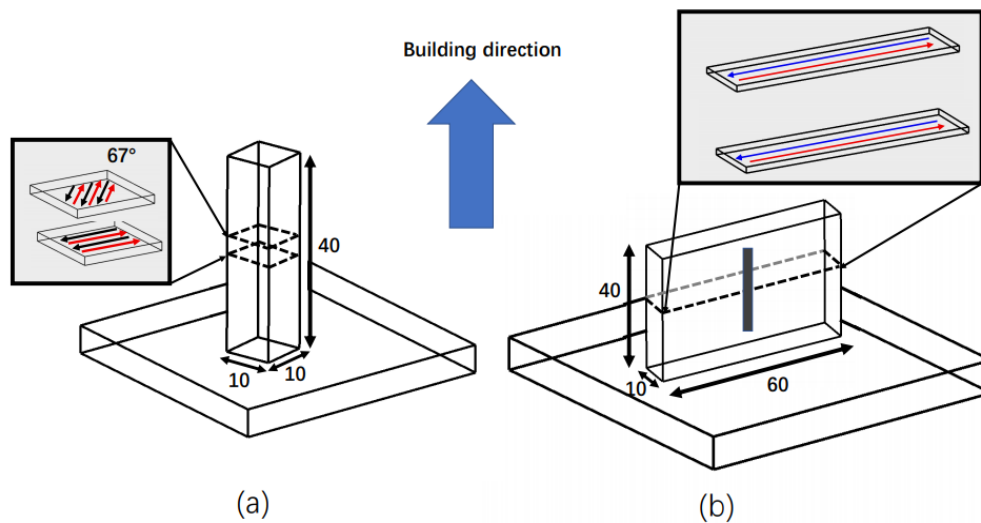| Code	Fe	Ni	Cr	Mn	Mo	Nb	Ti	Al	Cu	C	Si
LMD SS316L	Bal.	12.5	17.1	1.6	2.5	--	--	--	--	0.02	0.7
Com SS316L	Bal.	12.7	17.3	0.5	2.0	--	--	--	--	--	0.9
PBF-LB IN718	Bal.	50-55	17-21	0.35	2.8-3.3	4.74-5,.50	0.65-1.15	0.08-0.20	0.30	0.08	0.35
Com IN718	Bal.	46.4	17.4	0.2	4.6	4.8	1.0	1.2	--	--	--

Fig. 1 Dimensions of the (a) PBF-LB IN718 and (b) LMD SS316L, schematically detailing information on the building direction and scanning strategy.

2.2 Corrosion exposure experiment

A $MgCl_2$-KCl-NaCl (47.1-22.7-30.2 mol%, eutectic) salts mixture was employed for the corrosion test. The supplier of KCl (purity > 99 wt.%) and NaCl (purity > 99 wt.%) is Alfa Aesar, Germany. Anhydrous $MgCl_2$ (purity > 99 wt.%) was purchased from Magnesia, Germany. Considering the high hydration of the chloride salt, the salt was stored and weighed in a glove box (O_2 < 0.5 ppm, H_2O < 1 ppm) purged with Ar 5.0 (purity > 99.999 %). Figure 2 shows the set-up sketch of the corrosion experiment. Firstly, 250 g $MgCl_2$-KCl-NaCl was weighed in the glove box. Secondly, the chloride salt was loaded in the glass carbon crucible (Sigradur® G from HTW, Germany). This kind of crucible does not react with the salt at the given exposure temperature. The sample was cut in a dimension of 10 × 10 mm^2 with a thickness of 1 mm. All sample surfaces were grinded by sand paper with surface finish of 600# and 1200#, and then cleaned with alcohol. Afterwards, the sample was hung by a nickel wire. Each sample was isolated and fixed by an alumina tube to prevent floating during the exposure time (see in Fig. 2). Two samples of each composition were exposed to the same experimental condition. Before heating up the furnace, the system was cleaned and filled with Ar gas. The corrosion experiment was carried out under Ar gas at a flow rate of 10 L/h. The furnace was heated up to 700 °C (± 1 °C) with a heating rate of 10 K/min. The main corrosive impurity in the NaCl-KCl-$MgCl_2$ is $MgOH^+$. It has been measured based on titration and cyclic voltammetry (CV) experiments in accordance to [35]. The concentration of this type impurity is ~2000 ppm (5×10^{-2} mol/kg(salt)) after the salt mixture was heated up to 700 °C. After 500 hours (≈21 days) exposure, samples were cooled down within the furnace. Then, the samples covered by solid salts were extracted from the furnace and cleaned with distilled water.
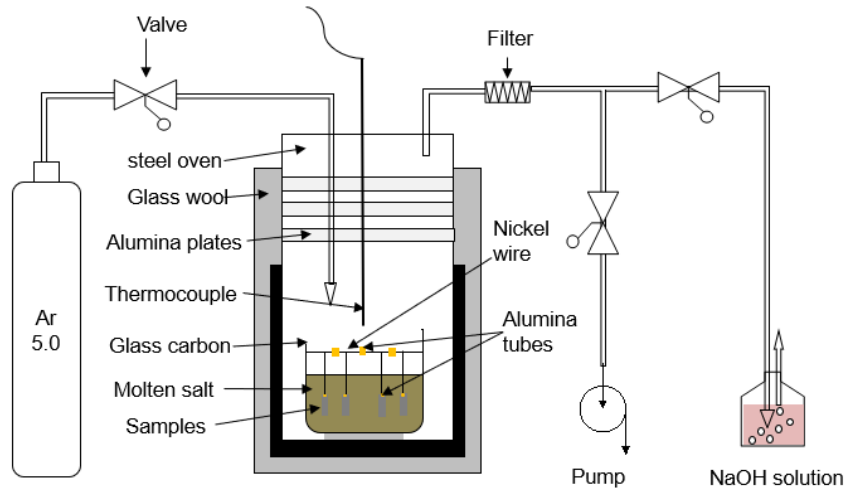
Fig. 2 Set-up used for the molten salt corrosion test.

2.3 Characterization

Both primary and exposed samples were characterized by Scanning Electron Microscopy (SEM) and X-Ray Diffraction (XRD). In case of cross section analysis, the samples were embedded in resin and ground with sand papers with the grit sizes 600#, 1200# and 2400#. Further polishing was performed by diamond paste with particle size of 1 μm in diameter. In addition, the sample surface was also deposited by a thin and conductive palladium (Pd) layer for the SEM analysis. The SEM used in the current study is a Zeiss LEO 1530 VP, equipped with an EDS unit. The energy of the electron beam is set to 10 and 20 keV, respectively, depending on the analysis conducted. Phase compositions have been characterized by XRD (Seifert PAD II) with Cu Kα1 radiation (λ=0.15406 nm, 40 kV and 30 mA) in Bragg–Brentano geometry (θ-2θ) with a step size of 0.02° and a scan speed of 0.1°/min. In addition, electron backscatter diffraction analysis (EBSD, Zeiss-Crossbeam XB 1540 focused ion beam-SEM instrument) was also conducted to further characterise the microstructure in the corroded regions.

3. Results

3. 1 Microstructure of primary alloys

Phase compositions of all samples were assessed by XRD and relevant data are shown in Fig. 3. The LMD SS316L shows signals from both austenite (PDF no. 33-397) and body-centred cubic (BCC) ferrite (weak, PDF no. 34-396). Peaks located at 2θ=45.5° and 65° correspond to the ferrite (marked by triangles in Fig. 3). For all other alloys, only the austenitic matrix-phase is resolved by XRD analysis.
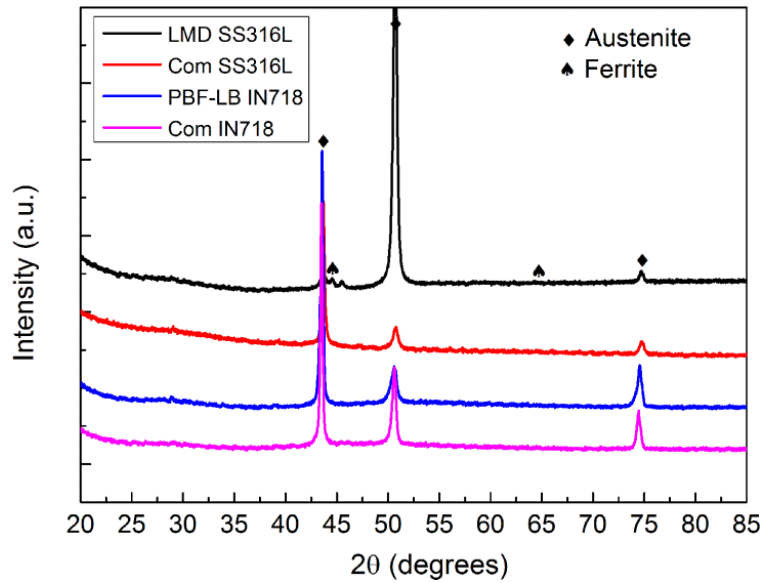
Fig. 3 XRD spectra of SS316L (LMD and commercial) and IN718 (PBF-LB and commercial) before corrosion testing (Com is abbreviation of commercial).

Fig. 4 displays SEM micrographs of all samples before the corrosion test. The precipitations at GBs are clearly visible in the matrix of the LMD SS316L sample. The EDS analysis indicates that the segregated regions are enriched in Cr and Mo, these elements being assigned to the δ-ferrite phase (PDF no. 34-396) according to the XRD results in Fig. 3. SS316L is prone to the formation of δ-ferrite, as has been reported in literature as well [28-29]. Besides, some pores/inclusions shown in dark contrast are distributed within the alloy matrix. Such pores are well-known defects in AM materials [17, 19]. In contrast, the commercial SS316L is characterised by uniform grain morphology and a homogeneous chemical composition, respectively. The SEM micrograph of PBF-LB condition shows a cell-like network, which is the result of the specific cooling condition in powder bed fusion process and also described in literature [36]. In comparison, the conventionally processed IN718 reveals grain morphologies and secondary phase like the needle shaped precipitates distributed uniformly in the whole matrix, see Fig. 4 (d). These precipitates are not resolved by XRD due to their low volume fraction. However, the EDS analysis confirms a local enrichment of Ni and Nb. In fact, the precipitates represent the $NbNi_3$ δ-phase being well-known in IN718 alloy [37]. Many other secondary phases being formed upon processing and heat treatments in IN718 are enriched in Nb as well. However, only the δ-phase is characterised by such kind of morphological appearance. In case of conventionally processed IN718, δ-phase is very important for controlling grain growth. However, δ-phase is not seen in PBF-LB IN718 in as-built conditions [38-39]. Besides, some inclusions and pores are seen in the PBF-LB IN718 as expected in case of any AM material.
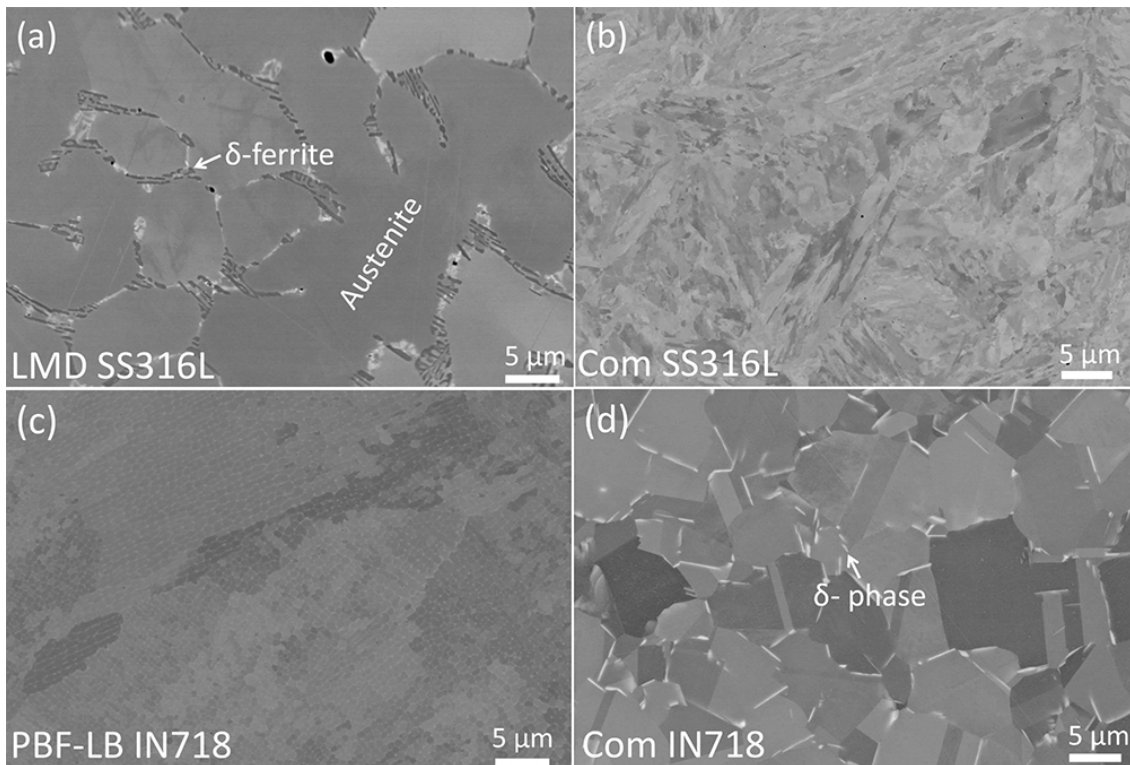
Fig. 4 Representative microstructures of AM and commercially processed alloys before corrosion testing (SS316L and IN718) obtained by SEM characterization.

3.2 Corrosion behavior

3.2.1 XRD characterization

Fig. 5 shows the EDS spectra highlighting the phase composition of all tested alloy conditions after the corrosion exposure at 700 °C for 500 h. After direct comparison with the primary materials (c.f. Fig. 3), new phases like MgO (PDF no. 87-652), and $NbNi_3$ (PDF no. 65-589) are identified. For instance, the main phases (potential effects stemming from texture are not considered here) obtained from the LMD SS316L include austenite (PDF no. 33-397), ferrite (PDF no. 34-396) and MgO. Additional peaks are related to the remaining adherent salts like $MgCl_2$, KCl and $NaMgCl_3$, which are represented by the $MgCl_2$ -NaCl-KCl salt peaks. These results are also confirmed for the conventionally processed SS316L, being characterised by the same main phases. The PBF-LB processed and commercial IN718 samples also show changes in terms of phase compositions in comparison to the primary material. Phases seen after the corrosion include austenite, $NbNi_3$ and MgO. The Nb-rich $NbNi_3$ phase, which is not resolved by XRD in the primary alloys, is clearly identified after the corrosion exposure and can be rationalised by the high-temperature exposure being in a range well-known for promoting formation of $NbNi_3$-phases, i.e., γ''-phase and δ-phase [38-39]. Table 2 summarizes the phase compositions of each sample after the corrosion exposure qualitatively.
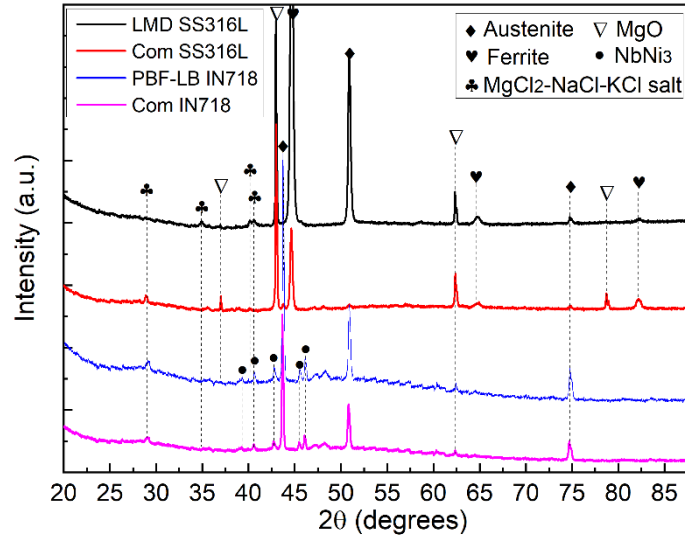
Fig. 5 XRD spectra of SS316L (LMD and commercial) and IN718 (PBF-LB and commercial) after exposure to molten MgCl₂-KCl-NaCl salts at 700 °C for 500 h under Ar atmosphere. The MgCl₂-NaCl-KCl salt peak represents peaks from MgCl₂, KCl and NaMgCl₃.

Table 2

Qualitative phase compositions of all samples after the corrosion exposure as determined by XRD.

Sample	Austenite	Ferrite	MgO	NbNi₃	Others
LMD SS316	+	+	+	-	MgCl₂, KCl NaMgCl₃
Com SS316	+	+	+	-	KCl, NaMgCl₃
PBF-LB IN718	+	-	+	+	MgCl₂, KCl, NaMgCl₃
Com IN718	+	-	+	+	MgCl₂, KCl

+: yes; -: no.

3.2.2 Surface morphology

Fig. 6 (a) presents the surface morphology of LMD SS316L after corrosion testing characterised by SEM. The metal surface highlighting different aspects is depicted by the magnified image of Fig. 6 (e). The major part of the surface shows bright contrast. EDS measurements reveal the enrichment of O, Fe, Mo and Ni. The Cr (≈ 3 wt.%) and Mn (< 1 wt.%) concentrations are lower than in the bulk alloy. In addition, a significant amount of dark precipitates, either present in the form of a "shell" structure or small round particles, are distributed alongside the bright regions. These precipitates, enriched in O and Mg, are due to the formation of MgO. The surface profile of commercial SS316L is shown in Fig. 6 (b). The sample surface is partially covered by a shell-like layer, shown in dark contrast. The shell structure is characterised by the enrichment of O and Mg. In contrast, the bright part is the metal

surface, which has no traces of O and Mg. However, the Cr is depleted in the whole surface, with around 2 wt.%, this value being much lower than in the bulk material. Fig. 6 (c) shows the general surface profile of PBF-LB IN718 after the corrosion test. Small pores with diameters of 1-2 µm are seen on the whole surface. The holes are induced by the corrosion attack. According to the difference in terms of morphology of the holes (shown details in Fig. 6 (f)), the corroded surface can be divided into two regions: the dense region with large pores (around 2 µm, region A), and the porous region with small pores (around 1 µm, region B). In contrast, the surface of commercial IN718 is characterised by pores, which are distributed uniformly across the whole surface, see Fig. 6 (d, g). No large pores, as those observed on PBF-LB IN718, can be identified. This kind of surface morphology is well-known from many steels/superalloys after being exposed to molten salts [4, 34]. Besides, EDS measurements (not shown) indicate the depletion of Cr on the metal surface.
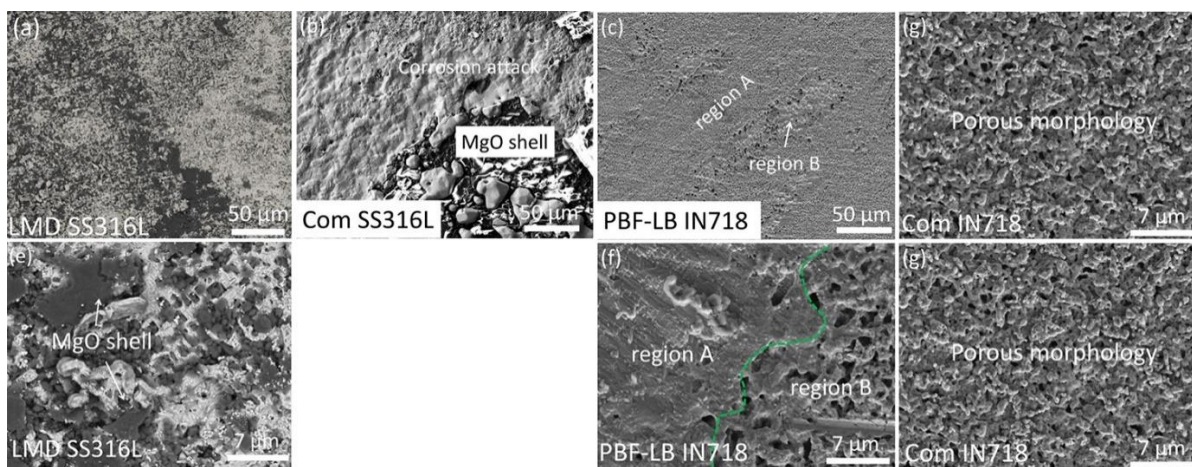

Fig. 6 Surface morphologies of tested materials after exposure to molten chloride salts at 700 °C for 500 h characterized by SEM; (a) LMD SS316L, (b) commercial SS316L, (c) PBF-LB IN718, (d) commercial IN718, (e) magnified LMD SS316L, (f) magnified PBF-LB IN718 and (g) magnified commercial IN718. See text for details.

3.2.3 Cross-sectional analysis

To establish the most relevant process-microstructure-corrosion relationship, the cross sections of all samples have been characterized. Fig. 7 (a) displays a cross-sectional overview image of the LMD SS316L. Pores are visible at the upper part of the cross section, with a corrosion depth of around 150-190 µm. Moreover, a careful analysis indicates that the corrosion preferentially prevails at certain regions. This kind of localised attack is related to the δ-ferrite being present at grain boundaries. Parts of these GBs precipitates seem to be replaced by pores. An EDS measurement indicates a depletion of Cr and also Mn at the corroded regions. Instead, O and Mg are enriched in the pore due to the precipitation of MgO [4]. Other elements, like Mo (at GBs), are hardly affected and still enriched within corroded regions.

To further reveal the relation between the phase distribution and the corrosion attack, an EBSD analysis has been performed within the corroded region of LMD SS316L, shown in Fig. 7 (c). The EBSD

phase map indicates that the alloy matrix is austenite, while the δ-ferrite (green coloured) is mainly located at GBs (Fig. 7 (d)). Moreover, corrosion induced pores, shown in dark contrast, are formed within the δ-ferrite phase.
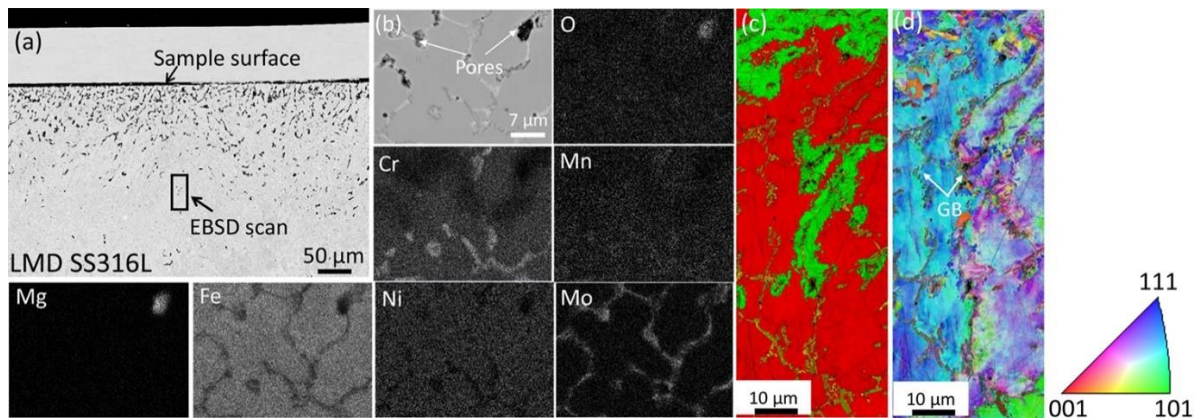

Fig. 7 SEM-EDS analysis of the cross section of LMD SS316L after 500 h exposure to molten chloride salts at 700 °C, (a) cross sectional overview image; (b) EDS elemental mapping; (c) EBSD phase map of the cross section (red colour: austenite; green colour: δ-ferrite); (d) EBSD IPF+IQ map of the cross sectional area marked on (a).

Fig. 8 displays the cross section of the conventionally processed SS316L. Although the microstructure is different from that of LMD SS316L, similarities in terms of the corrosion behavior prevail. Both Cr and Mn are depleted while MgO precipitates are seen in corroded regions. The surface of the steel is covered by a MgO layer. However, some differences in the corrosion behavior are also obvious. For instance, the corroded region (around 70 μm) is not as thick as in case of the LMD SS316L. Furthermore, the corrosion depth is nearly uniform.

To precisely understand what happens within corroded regions, the cross section has been further characterized by EBSD. The EBSD phase map depicted in Fig. 8 (c) reveals that ferritization is enabled within corroded regions (bcc phase marked with green colour). This result clearly confirms the XRD measurement, where signals only stem from the volumes being in direct vicinity of the sample surface. As is indicated by the SEM analysis, corrosion attack most probably starts from GBs. However, large pores being present in some regions do not allow for final conclusion here.
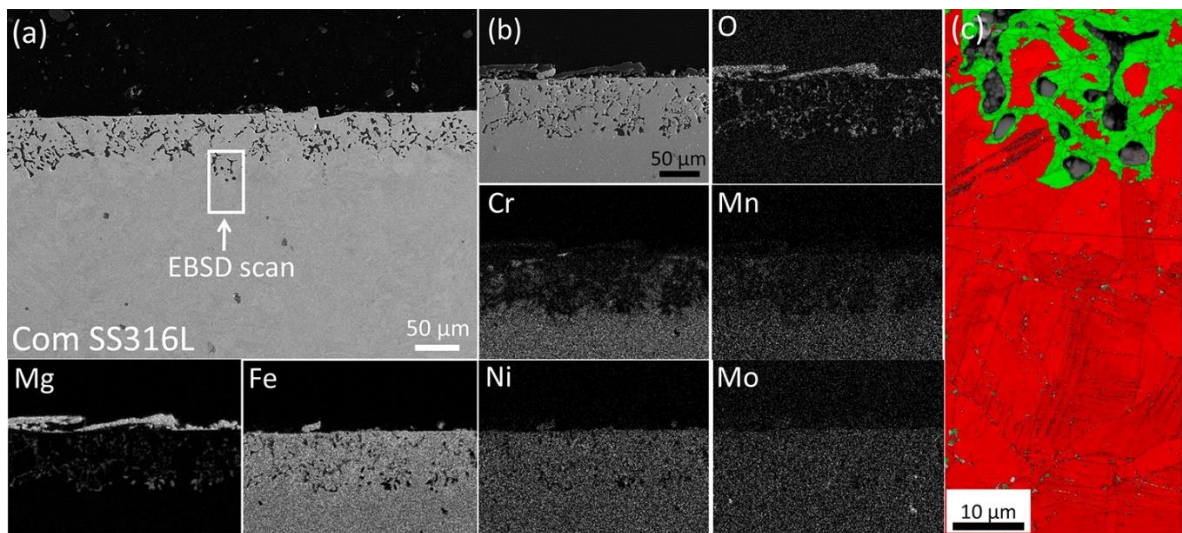
Fig. 8 SEM-EDS analysis of the cross section of conventionally processed SS316L after 500 h exposure to molten chloride salts at 700 °C, (a) cross section overview image; (b) EDS elemental mapping; (c) EBSD phase map of the cross section (red colour: austenite; green colour: ferrite).

The cross section of the PBF-LB IN718 is shown in Fig. 9. Generally, two types of corrosion morphologies can be recognized: one type with uniform corrosion and a second type of the grain boundary/precipitate driven corrosion. The Cr is depleted, especially more visible at the second type corrosion. The first type is characterised by features such as small and dense pores. It is only formed at the region adjacent to the sample surface, with a corrosion depth around 15 μm. This appearance clearly corresponds to the surface morphology observed within region A (Fig. 6), while the second type is prone to formation of larger pores, which is consistent with the region B (Fig. 6). However, the second type corrosion pores form on the whole corroded region and penetrate to a large depth varying from 65 to 95 μm. In addition, a simultaneous accumulation of Nb is observed along GBs, adjacent to the corroded pores, is seen concomitantly. This clearly indicates the precipitation and growth of the second phase alongside GBs, which is corresponding to the δ-phase. The precipitates in the alloy matrix are needle shape while large block type precipitates are observed at GBs (see Fig. 9 (b)). Moreover, the corrosion attack mainly appears at GBs, as indicated by the holes being present in the image. It is assumed that the corrosion attack is initiated at the interface of the alloy matrix and the large block type δ-phase precipitates at GBs. However, further experiments are needed to clarify this aspect, i.e. time-resolved evolution of corrosion attack.
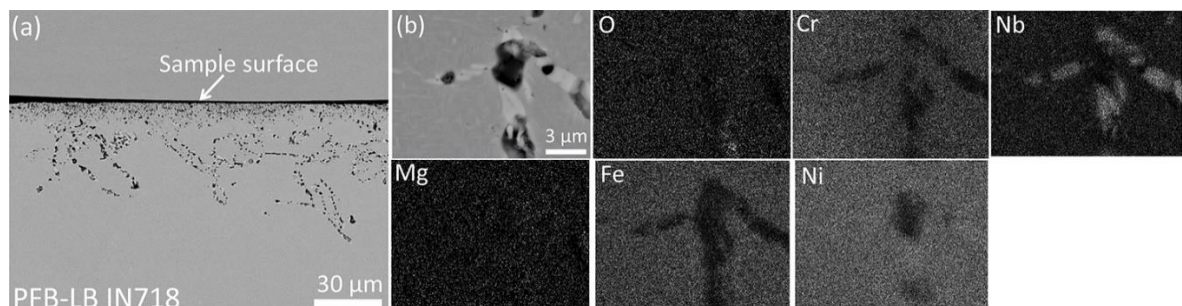
Fig. 9 SEM-EDS analysis of the cross section of PBF-LB IN718 after 500 h exposure to molten chloride salts at 700 °C, (a) cross section overview image; (b) EDS elemental mapping.

Fig. 10 shows cross-sectional images of conventionally processed IN718. As in case of the PBF-LB IN718, two types of corroded morphologies are identified, being characterised by uniform corrosion and corrosion along GBs. The uniform corrosion, close to the sample surface, leads to the formation of smaller pores. The second type corrosion is restricted to the GBs, as highlighted by the pores penetrating into the bulk material. Instead of fine precipitates, large blocks of secondary phase are visible alongside the corroded GBs, which are enriched in Nb according to the EDS mappings. Besides, the mapping reveals the depletion of Cr in case of both types of corrosion attacks. MgO precipitates are visible in corrosion induced pores. The first type corrosion is characterised by a depth effect of 10 µm while the total corrosion depth is in the range of 40-55 µm. Furthermore, the cross section was also probed by EBSD. The red coloured region is austenitic while the green coloured region is assigned to NbNi$_3$ phase (in line with results obtained by XRD and SEM/EDS). The dark regions are pores induced by the corrosion attack. However, it seems that the location of corroded pores is more easily identified from the BSE image (Fig. 10 (d)).
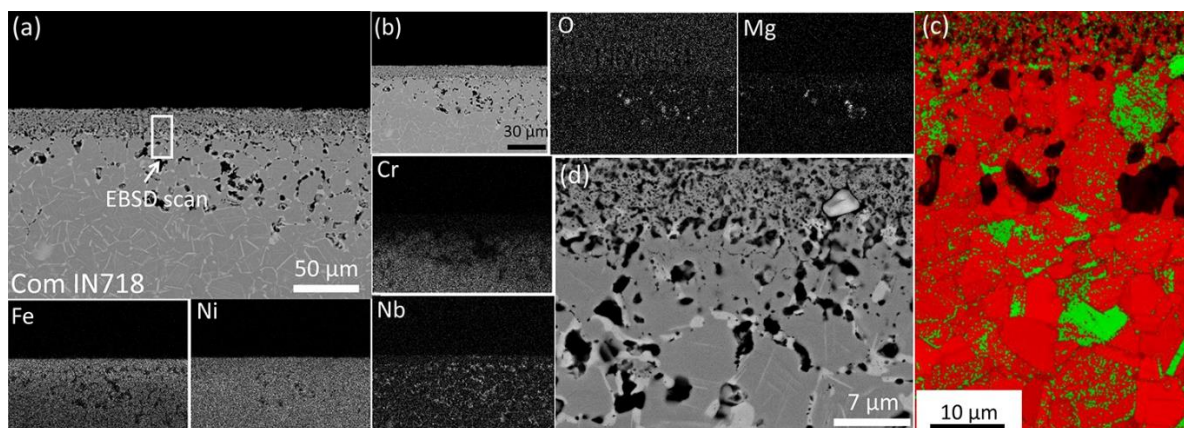

Fig. 10 SEM-EDS analysis of the cross section of conventionally processed IN718 after 500 h exposure to molten chloride salts at 700 °C, (a) cross section overview image; (b) EDS elemental mapping; (c) EBSD phase map of the cross section (red colour: Austenite; green colour: NbNi$_3$ phase); (d) magnified cross section.

4. Discussion

In direct comparison to wrought/forged SS316L and IN718 counterparts, the alloys processed by LMD and PBF-LB are characterised by distinct microstructural features: phase segregation, inhomogeneity in terms of local composition and defects induced by the final process. Some of these phases/regions/characteristics are expected to promote localised corrosion attack. This is clearly experimentally revealed in present work. Generally, the corrosion resistance of AM SS316L is inferior to that of conventionally processed counterparts when exposed to molten chloride salts. This is mainly reflected by the deeper corrosion depth and the increased second phase/GBs accelerated corrosion

attack. The corrosion depth of IN718 produced by different methods (PBF-LB and wrought/forged) are almost similar in general corrosion region (15 µm vs. 10 µm) while the grain boundary corrosion is enhanced with PBF-LB sample (65-95 µm vs. 40-55 µm). The corrosion depth of LMD SS316L is almost two times higher than in case of the conventionally processed SS316L. Obviously, the different behavior of these two types of materials (SS316L and IN718) is promoted by different corrosion mechanisms.

As a major contributing corrosion mechanism proposed in recent papers focusing on conventionally processed materials [4-7], selective leaching of active elements such as Cr and Mn is also observed in the AM materials here. Moreover, the corrosion mechanism being active in AM steels and superalloys is more complex than the commercial counterpart. This is mainly due to the segregation of secondary phases/precipitates at GBs.

Specifically, the corrosion attack of LMD SS316L is negatively influenced by the δ-ferrite segregated at GBs. Since the ferrite phase is enriched in Cr and Fe, it is expected to accelerate the corrosion attack because of a relatively high EMF value (theoretical standard electromotive force) [4, 11]. Moreover, the fast diffusion of elements through GBs also enhances the intergranular corrosion attack. Furthermore, it is observed that the volume fraction of δ-ferrite increases after the corrosion exposure. This might be caused by the dissolution of austenite stabilizers like Mn. As for commercial SS316L, the ferrite phase has also been observed after corrosion exposure, which can share the same reason for ferritization, namely the selective leaching of austenite stabilizers. However, the depth of corroded region is less pronounced in the conventionally processed SS316L since no fast diffusion path is provided by the Cr-rich δ-ferrite phase formed on GBs. Due to the decoration of GBs with the δ-ferrite phase directly induced by LMD (cf. Fig. 4), fast diffusion paths prevail in the LMD SS316L already in the as-built condition rationalizing the more pronounced corrosive in-depth effect.

In case of IN718, two different corrosion morphologies including the uniform corrosion and precipitates/GBs accelerated corrosion are identified, respectively. These can be rationalised based on the contribution of two different corrosion mechanisms. Both types of corrosion attacks are observed in PBF-LB and conventionally processed IN718 alloys. The mechanism of the uniform corrosion attack is known from many other Ni-based alloys, being related to the preferential dissolution of elements with high EMF value like Cr and Mn [11]. Both samples show similarities in terms of the corrosion depth of this type corrosion. The second type corrosion is mainly promoted by the GB effect as well as precipitates at GBs. Firstly, GBs provide a fast route either for inward corrosive ions or outward metallic elements diffusion. Secondly, the segregation of δ-phase at GBs results in the local enrichment of Cr and Fe, eventually accelerating the corrosion attack in chloride salts. Moreover, the depletion of Cr (due to corrosion) further promotes the clustering of Nb-rich phases, which might explain the very

pronounced coarsening of the δ-phase (NbNi$_3$) especially at GBs in the corroded regions. In fact, the coarsening of δ-phase is less pronounced in non-corroded regions. Such locally promoted growth of the NbNi$_3$-phase is also reported in literature [40]. Besides, the PBF-LB IN718 shows significantly larger depth of the second type of corrosion within some specific regions when compared with the commercial IN718. This might be related to well-known AM process induced defects like inclusions and pores, eventually accelerating the corrosion attack [19, 20, 24]. However, time-resolved analysis of evolution of corrosion induced damage will be the subject of future studies.

Finally, when comparing the corrosion resistance of the AM materials in focus, the PBF-LB IN718 is more corrosion resistant than the LMD SS316L when exposed to molten chloride salts environment. As is explained in previous work focusing on conventionally processed counterparts, this is mainly due to the higher Ni and lower Cr contents in IN718 [4, 15, 11]. The inferior corrosion performance seen in case of the AM processed materials is mainly due to the unique microstructure evolution and process induced material defects. Both AM processed materials have been assessed in as-built conditions. Thus, many types of target-oriented heat treatments can be considered to mitigate the segregations and material defects. Based on the results elaborated and discussed in present work, this will be clearly helpful to significantly improve their corrosion performance of the AM alloys. Microstructures of the AM processed conditions will be tailored to be able to withstand corrosive attack more effectively. Direct microstructure control and/or adequate post heat treatments have to be established to meet demands in envisaged fields.

5. Conclusions

In the present work, laser powder bed fusion (PBF-LB) and laser metal deposition (LMD), being two well-established types of AM technologies, were employed for processing of stainless steel 316L (SS316L) and Ni-base superalloy Inconel 718 (IN718). AM and conventionally processed samples were assessed by corrosion tests, where the samples were exposed to MgCl$_2$-KCl-NaCl (47.1-22.7-30.2 mol%) salts at 700 °C under Ar atmosphere.

Based on the results presented, the following conclusions can be obtained:

(a) The corrosion performance of LMD SS316L is inferior to the commercial SS316L, while PBF-LB IN718 shows a corrosion resistance similar to the commercial IN718;

(b) The segregated δ-ferrite at GBs of LMD SS316L is prone to localised corrosion attack, which is due to the enrichment of Cr and Fe. Moreover, ferritization is observed in corroded regions of both LMD processed and commercial SS316L.

(c) Two types of corrosion attack, namely uniform corrosion and grain boundary/precipitates driven corrosion, are observed in the IN718 alloys (PBF-LB and commercial). The fast diffusion of alloying elements promoted by GBs and precipitates at GBs promotes the GB driven

corrosion attack.

Data availability

The raw/processed data required to reproduce these findings cannot be shared at this time due to technical or time limitations. The datasets obtained in the present study are available from the corresponding author on reasonable request.

Acknowledgements

Reference

[1]   D. Neil, H. Clark, R. Wiswall Jr, Thermodynamic Properties of Molten Solutions of $MgCl_2$-KCl, $MgCl_2$-NaCl, and $MgCl_2$-KCl-NaCl, J. Chem. amp; Eng. Data 10 (1965) 21-24.

[2]   D. Williams, Assessment of candidate molten salt coolants for the NGNP/NHI heat-transfer loop, in, Oak Ridge National Lab (ORNL), Oak Ridge, TN (United States), 2006.

[3]   W. Ding, T. Bauer, Progress in Research and Development of Molten Chloride Salt Technology for Next Generation Concentrated Solar Power Plants, Engineering, (2021).

[4]   W. Ding, H. Shi, Y. Xiu, A. Bonk, A. Weisenburger, A. Jianu, T. Bauer, Hot corrosion behavior of commercial alloys in thermal energy storage material of molten $MgCl_2$/KCl/NaCl under inert atmosphere, Sol. Energy Mater Sol. Cells 184 (2018) 22-30.

[5]   S. Guo, J. Zhang, W. Wu, W. Zhou, Corrosion in the molten fluoride and chloride salts and materials development for nuclear applications, Prog. Mater. Sci. 97 (2018) 448-487.

[6]   H. Sun, J. Wang, Z. Li, P. Zhang, X. Su, Corrosion behavior of 316SS and Ni-based alloys in a ternary NaCl-KCl-$MgCl_2$ molten salt, Sol. Energy 171 (2018) 320-329.

[7]   H. Sun, P. Zhang, J. Wang, Effects of alloying elements on the corrosion behavior of Ni-based alloys in molten NaCl-KCl-$MgCl_2$ salt at different temperatures, Corros. Sci. 143 (2018) 187-199.

[8]   J. W. Wang, H. X. Zhou, C. Z. Zhang, W. N. Liu, B. Y. Zhao, Influence of $MgCl_2$ content on corrosion behavior of GH1140 in molten NaCl-$MgCl_2$ as thermal storage medium, Sol. Energy Mater. Sol. Cells 179 (2017) 194-201.

[9]   B.A. Pint, J.W. McMurray, A.W. Willoughby, J.M. Kurley, S.R. Pearson, M.J. Lance, D.N. Leonard, H.M. Meyer, J. Jun, S.S. Raiman, Re-establishing the paradigm for evaluating halide salt compatibility to study commercial chloride salts at 600 - 800 °C, Mater. Corros. 70 (2019) 1439-1449.

[10]   A.R. Shankar, U.K. Mudali, Corrosion of type 316L stainless steel in molten LiCl–KCl salt, Mater. Corros. 59 (2008) 878-882.

[11] W. Ding, H. Shi, A. Jianu, Y. Xiu, A. Bonk, A. Weisenburger, T. Bauer, Molten chloride salts for next generation concentrated solar power plants: Mitigation strategies against corrosion of structural materials, Sol. Energy Mater. Sol. Cells 193 (2019) 298-313.

[12] W. Ding, A. Bonk, J. Gussone, T. Bauer, Electrochemical measurement of corrosive impurities in molten chlorides for thermal energy storage, J. Energy Storage 15 (2018) 408-414.

[13] W. Ding, A. Bonk, T. Bauer, Corrosion behavior of metallic alloys in molten chloride salts for thermal energy storage in concentrated solar power plants: A review, Front. Chem. Sci. Eng. 12 (2018) 564-576.

[14] J. Gomez-Vidal, A. Fernandez, R. Tirawat, C. Turchi, W. Huddleston, Corrosion resistance of alumina-forming alloys against molten chlorides for energy production. I: Pre-oxidation treatment and isothermal corrosion tests, Sol. Energy Mater. Sol. Cells 166 (2017) 222-233.

[15] J. Zhang, C.W. Forsberg, M.F. Simpson, S. Guo, S.T. Lam, R.O. Scarlat, F. Carotti, K.J. Chan, P.M. Singh, W. Doniger, Redox potential control in molten salt systems for corrosion mitigation, Corros. Sci. 144 (2018) 44-53.

[16] W. Ding, T. Bauer, Progress in Research and Development of Molten Chloride Salt Technology for Next Generation Concentrated Solar Power Plants, Engineering (2021).

[17] I. Gibson, D. Rosen, B. Stucker, M. Khorasani, Additive manufacturing technologies. New York: Springer 17 (2014) 195.

[18] D. Herzog, V. Seyda, E. Wycisk, C. Emmelmann, Additive manufacturing of metals, Acta Mater. 117 (2016) 371-392.

[19] G. Sander, J. Tan, P. Balan, O. Gharbi, D. Feenstra, L. Singer, S. Thomas, R. Kelly, J.R. Scully, N. Birbilis, Corrosion of additively manufactured alloys: a review, Corrosion 74 (2018) 1318-1350.

[20] A.H. Ettefagh, S. Guo, J. Raush, Corrosion performance of additively manufactured stainless steel parts: A review, Addit. Manuf. (2020) 101689.

[21] D. Gu, X. Shi, R. Poprawe, D.L. Bourell, R. Setchi, J. Zhu, Material-structure-performance integrated laser-metal additive manufacturing, Science 372 (2021).

[22] Y. Zhong, L.-E. Rännar, L. Liu, A. Koptyug, S. Wikman, J. Olsen, D. Cui, Z. Shen, Additive manufacturing of 316L stainless steel by electron beam melting for nuclear fusion applications, J. Nucl. Mater. 486 (2017) 234-245.

[23] M. Lodhi, K. Deen, W. Haider, Corrosion behavior of additively manufactured 316L stainless steel in acidic media, Materialia 2 (2018) 111-121.

[24] G. Asala, J. Andersson, O.A. Ojo, Hot corrosion behaviour of wire-arc additive manufactured Ni-based superalloy ATI 718Plus®, Corros. Sci. 158 (2019) 108086.

[25] C. Juillet, A. Oudriss, J. Balmain, X. Feaugas, F. Pedraza, Characterization and oxidation resistance of additive manufactured and forged IN718 Ni-based superalloys, Corros. Sci. 142 (2018) 266-276.

[26] G.S. Mahobia, N. Paulose, S. Mannan, R. Sudhakar, K. Chattopadhyay, N.S. Srinivas, V. Singh, Effect of hot corrosion on low cycle fatigue behavior of superalloy IN718, Int. J. Fatigue 59 (2014) 272-281.

[27] T. Sanviemvongsak, D. Monceau, B. Macquaire, High temperature oxidation of IN 718 manufactured by laser beam melting and electron beam melting: Effect of surface topography, Corros. Sci. 141 (2018) 127-145.

[28] M. Ziętala, T. Durejko, M. Polański, I. Kunce, T. Płociński, W. Zieliński, M. Łazińska, W. Stępniowski, T. Czujko, K.J. Kurzydłowski, The microstructure, mechanical properties and corrosion resistance

of 316 L stainless steel fabricated using laser engineered net shaping, Mater. Sci. Eng. A 677 (2016) 1-10.

[29] X. Li, J. Shi, C. Wang, G. Cao, A. Russell, Z. Zhou, C. Li, G. Chen, Effect of heat treatment on microstructure evolution of Inconel 718 alloy fabricated by selective laser melting, J. Alloys Compd. 764 (2018) 639-649.

[30] P. Kanagarajah, F. Brenne, T. Niendorf, H. Maier, Inconel 939 processed by selective laser melting: Effect of microstructure and temperature on the mechanical properties under static and cyclic loading, Mater. Sci. Eng. A 588 (2013) 188-195.

[31] A.B. Rhouma, T. Amadou, H. Sidhom, C. Braham, Correlation between microstructure and intergranular corrosion behavior of low delta-ferrite content AISI 316L aged in the range 550 - 700 °C, J. Alloys Compd. 708 (2017) 871-886.

[32] X. Zhuang, W. Liu, X. Xu, Hot corrosion of different alloys in chloride and carbonate molten-salt mixtures under argon atmosphere, Sol. Energy 189 (2019) 254-267.

[33] N.S. Patel, V. Pavlík, B. Kubíková, M. Nosko, V. Danielik, M. Boča, Corrosion behaviour of Ni-based superalloys in molten FLiNaK salts, Corros. Eng. Sci. Technol. 54 (2019) 46-53.

[34] B. Aminforoughi, S. Degener, J. Richter, A. Liehr, T. Niendorf, A Novel Approach to Robustly Determine Residual Stress in Additively Manufactured Microstructures Using Synchrotron Radiation, Adv. Eng. Mater. 23 (2021) 2100184.

[35] W. Ding, A. Bonk, J. Gussone, T. Bauer, Cyclic voltammetry for monitoring corrosive impurities in molten chlorides for thermal energy storage, Energy Procedia 135 (2017) 82–91.

[36] J.L. Bartlett, X. Li, An overview of residual stresses in metal powder bed fusion, Addit. Manuf. 27 (2019) 131-149.

[37] S. Mahadevan, S. Nalawade, J.B. Singh, A. Verma, B. Paul, K. Ramaswamy, Evolution of δ phase microstructure in alloy 718, in: Proceedings of the 7th International Symposium on Superalloy, 2010.

[38] M.E. Aydinöz, F. Brenne, M. Schaper, C. Schaak, W. Tillmann, J. Nellesen, T. Niendorf, On the microstructural and mechanical properties of additively manufactured Inconel 718 superalloy under quasi-static and cyclic loading, Mater. Sci. Eng. A 669 (2016) 246-258.

[39] M. Pröbstle, S. Neumeier, J. Hopfenmüller, L.P. Freund, T. Niendorf, D. Schwarze, M. Göken, Superior creep strength of a nickel-based superalloy produced by selective laser melting, Mater. Sci. Eng. A 674 (2016) 299-307.

[40] Q. Zhang, J. Zhang, Y. Zhuang, J. Lu, J. Yao, Hot Corrosion and Mechanical Performance of Repaired Inconel 718 Components via Laser Additive Manufacturing, Materials 13 (2020) 2128.